JFM RAPIDS
journals.cambridge.org/rapids

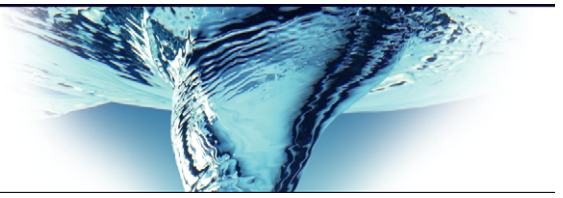

Experimental evidence of convective and absolute instabilities in rotating Hagen–Poiseuille flow

K. Shrestha[1], L. Parras[1], C. Del Pino[1,†], E. Sanmiguel-Rojas[2] and R. Fernandez-Feria[1]

[1]Fluid Mechanics, Universidad de Málaga, E.T.S. Ingeniería Industrial, Campus de Teatinos, 29071, Málaga, Spain

[2]Department of Mechanics, Universidad de Córdoba, E. Politécnica Superior, Campus de Rabanales, 14071, Córdoba, Spain

(Received 14 August 2012; revised 26 November 2012; accepted 1 December 2012)

Experimental results for instabilities present in a rotating Hagen–Poiseuille flow are reported in this study through fluid flow visualization. First, we found a very good agreement between the experimental and the theoretical predictions for the onset of convective hydrodynamic instabilities. Our analysis in a space–time domain is able to obtain quantitative data, so the wavelengths and the frequencies are also estimated. The comparison of the predicted theoretical frequencies with the experimental ones shows the suitability of the parallel, spatial and linear stability analysis, even though the problem is spatially developing. Special attention is focused on the transition from convective to absolute instabilities, where we observe that the entire pipe presents wavy patterns, and the experimental frequencies collapse with the theoretical results for the absolute frequencies. Thus, we provide experimental evidence of absolute instabilities in a pipe flow, confirming that the rotating pipe flow may be absolutely unstable for moderate values of Reynolds numbers and low values of the swirl parameter.

Key words: absolute/convective instability, instability

1. Introduction

Rotating pipe flows are of great interest both theoretically, mainly for their fundamental and intriguing stability properties (see the next paragraph), and because there are many engineering applications in which rotation plays an important role, for instance diffusion flames supported by rotating burners (Hossain, Jackson & Buckmaster 2009) or a new generation of swirl-inducing pipes that have improved transportation of particle-bearing liquids (Ariyaratne & Jones 2007). Furthermore,

† Email address for correspondence: cpino@uma.es

doi:10.1017/jfm.2012.600

the induced swirl in a sudden contraction of hydraulic systems (Sanmiguel-Rojas & Fernandez-Feria 2006) promotes the appearance of fluctuations in the flow rate when absolutely unstable conditions are reached (Sanmiguel-Rojas & Fernandez-Feria 2005). Though there are many works dealing with turbulent swirling pipe flows, the turbulent state or its transition from a laminar flow is outside the scope of the present work.

The stability of a fully developed rotating Hagen–Poiseuille pipe flow (RHPF) has been studied by several researchers theoretically. Although the non-rotating pipe Poiseuille flow is linearly stable for any finite Reynolds number, according to the temporal and linear stability analyses of Pedley (1968, 1969) and Mackrodt (1976), the introduction of rotation destabilizes the laminar flow at relatively low Reynolds numbers, becoming unstable to non-axisymmetric disturbances. These results were confirmed and extended by Cotton & Salwen (1981). A rotating pipe flow was found to be supercritically unstable both in the rapid- and slow-rotation regimes in Toplosky & Akylas (1988). These waves were later found in Barnes & Kerswell (2000) to become unstable to three-dimensional travelling waves in a supercritical Hopf bifurcation. To complement these results, a spatial, viscous and linear stability analysis of Poiseuille pipe flow with superimposed solid-body rotation was considered in Fernandez-Feria & del Pino (2002), where the convective or absolute character of the hydrodynamic instabilities in RHPF was also determined by examining the branch-point singularities of the dispersion relation for complex frequencies and wavenumbers (Huerre & Monkewitz 1990). Useful information from an experimental point of view related to wavelengths and frequencies associated with the neutral curve for the transition from stable to convectively unstable state was reported in Fernandez-Feria & del Pino (2002). The theoretical results confirmed that the wave packets corresponding to the most unstable modes were the slowest travelling along the pipe. As the Reynolds number, Re, or the swirl parameter, L, was increased (see the next section for the definition of Re and L), eventually the complex group velocity vanished to zero, resulting in the onset of the absolute instabilities. Thus, the transitional neutral curve from convective to absolute instabilities was characterized, covering all values of the parameters: Re, L, azimuthal wavenumber n, frequency ω and axial wavenumber α. This theoretical work was supplemented with three-dimensional numerical simulations in Sanmiguel-Rojas & Fernandez-Feria (2005), finding a good agreement in relation to the theoretical neutral curves. The flow rate oscillations and the nonlinear wave structures were also analysed in detail. Subsequently, Heaton (2008) described exhaustively the different instability typologies for RHPF, and a novel theory developed to study trailing line vortices was applied successfully to connect high- and low-swirl-parameter regimes (see references therein for more details).

The first experimental analysis of rotating pipe flow was by White (1964), Nagib, Lavan & Fejer (1971) and Mackrodt (1976), who found that rotation destabilizes the laminar flow and non-axisymmetric instabilities appeared. Later Imao *et al.* (1992) focused their experiments on the developing region of the axially rotating pipe. Only one Reynolds number and several values of the swirl parameter were tested in this work. The wavelengths and frequencies observed experimentally were later validated theoretically using a non-parallel approximation by means of the parabolized stability equations for developing RHPF in del Pino, Ortega-Casanova & Fernandez-Feria (2003).

Thus, to fill a gap in the experimental works on this problem, we analyse here the results for RHPF from an experimental point of view to link the observations with theoretically predicted convective and absolute instabilities. This is the main aim of the present work, which is organized as follows. In § 2 the experimental setup is described,

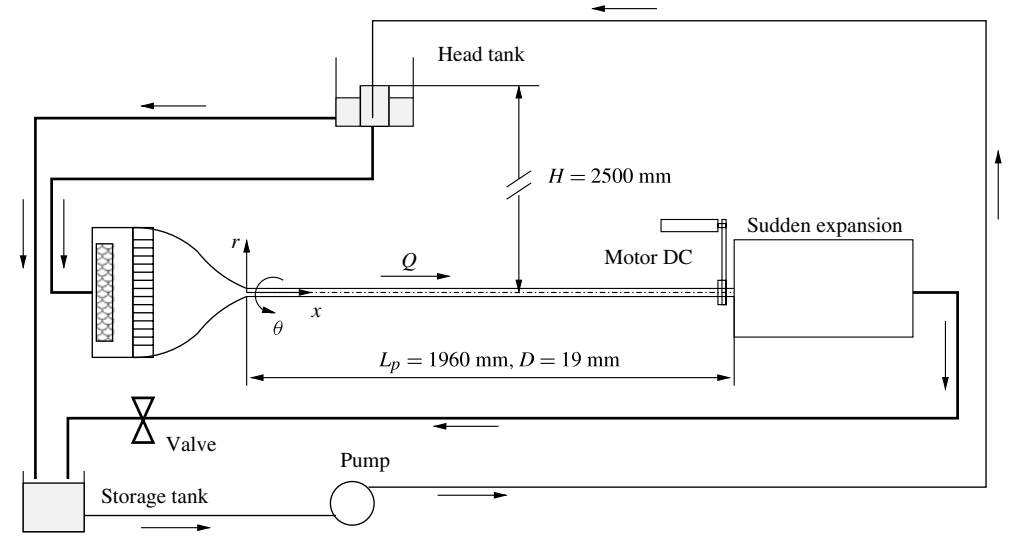

FIGURE 1. Sketch of the experimental setup.

together with a discussion of the flow geometry and the boundary conditions. In § 3 we show the experimental results for the transition from stable to convectively and absolutely unstable flows, and quantitative results for the frequencies and wavenumbers are also presented. In § 4 we sum up the main findings and draw some conclusions.

2. Experimental setup

We used the experimental setup depicted in figure 1, which allowed us to obtain the base RHPF in a horizontal pipe. The main parts were a head tank, a condition chamber, where a diffuser and a honeycomb were placed to reduce the noise at the pipe inlet, a pipe (diameter, $D = 19 \pm 0.04$ mm and length, $L_p = 1960$ mm), a DC motor and a storage tank. An aluminium structure was used to hold the experimental setup. The different sections were accurately aligned with a digital inclinometer to within $\pm 0.1°$.

A circulation system was employed and a transparent Perspex pipe was used for visualization that was recorded by a digital video camera. The water was pumped from the storage tank to the head (large) tank upstream of the pipe, which had other smaller tank inside. These small and large tanks were connected to the pipe and to the storage tank, respectively. Thus, the flow entered the smaller tank, and once this tank was filled, it started to fill the second tank that was connected to the storage tank. Thanks to this design, a pressure drop along the pipe was fixed by the constant height H between the small reservoir upstream (high level) and the inlet of the rotating pipe (low level). During each measurement a valve ensured a constant head loss in the hydraulic system. The value of H was 2500 mm, while the fluctuation in the small tank upstream was less than 2 mm, so that the accuracy of the flow rate was greater than 99.9 %. A similar experimental setup has been used in other works on pipe flows (see e.g. Hof *et al.* 2006). The water temperature was measured before and after each test to take into account the changes in the kinematic viscosity. The temperature

variation was less than 0.1 °C. The angular rotation was maintained constant by a DC motor connected to the pipe with a transmission belt. The motor was closed-loop controlled, and the velocity of the motor was known by means of an encoder. This feedback control was able to keep the error between the desired and the current angular velocities to within 0.5 %.

The test section was transparent to allow image recording. A light was projected on dark paper with a thin rectangular hole, forming a white light sheet vertically highlighting the flow patterns. To that end, Mearl Maid (flakes) or Kalliroscope was added to the fluid. To avoid flow disturbance downstream, a sudden expansion was connected at the end of the rotating pipe.

The Reynolds number is defined as $Re = UD/\nu = 4Q/(\pi D\nu)$, where U is the mean velocity, ν is the kinematic viscosity and Q is the flow rate. The swirl parameter is $L = \Omega D/(4U)$, Ω being the angular velocity. The final measured Reynolds number was constant within a variation of 0.5 %. Several series of experiments corresponding to Reynolds numbers ranging from 50 to 350 were performed and the swirl parameters were varied between 0 and 4. At least two runs for a given Re–L pair were carried out to ensure the reliability of the experimental results, and each experiment was running long enough to ensure final states. Finally, the pipe length, $L_P \approx 106D$, was also long enough to achieve RHPF for the values of Re and L considered here (see below).

3. Results and discussion

Typical flow visualizations in two windows along the pipe, one in the inlet region ($2D \lesssim x \lesssim 10.5D$) and the other one in the downstream region ($84D \lesssim x \lesssim 94D$), are shown in figure 2. Qualitative and quantitative analyses (described below) of flow visualizations like these for different values of Re and L, allowed us to obtain the critical values of Re and L for the onset of both convective and absolute instabilities, as well as their corresponding critical frequencies and wavenumbers. Due to the configuration of the experimental setup, the fluid entered the pipe without swirl, which developed along the entrance length. The first window always corresponds to this entrance length where the RHPF is not fully established, while the second corresponds, in all the cases reported here, to the fully developed RHPF. In Pedley (1969) it was reported that the minimum non-dimensional pipe length, $2L_p/D$, for achieving fully developed RHPF is of the order of the maximum between Re and Re_θ, where $Re_\theta \equiv ReL = \Omega D^2/(4\nu)$ is the Reynolds number based on the angular velocity. In our case, $2L_p/D \approx 212$, so that both Re and Re_θ have to be at most of this order in our experiments. However, this estimation is rather conservative and good agreement was found between theoretical frequencies and wavelengths for fully developed RHPF even for higher values of Re and Re_θ.

Figure 2(*a,b*) shows flow visualizations for a stable case, where one can observe the rotating boundary layer development region with an axisymmetric conical shape (ACS) in the inlet region (*a*), and no pattern in the downstream region (*b*). As the Reynolds or the swirl parameter was smoothly increased, new final states were reached, so the frames highlighted sinusoidal shapes in the downstream region (*d*) which represent convective travelling waves (see below), while the inlet region remained unaffected, with an ACS similar to the stable case (*c*). For higher values of L and moderate values of Re another transition occurred, breaking the symmetry of the ACS in the inlet region and leaving a spiral structure over the conical shape (*e*) (steady wavy cone, or SWC for short), while the downstream region (*f*) showed a sinusoidal structure qualitatively similar to the previous case (*d*). We shall argue below that

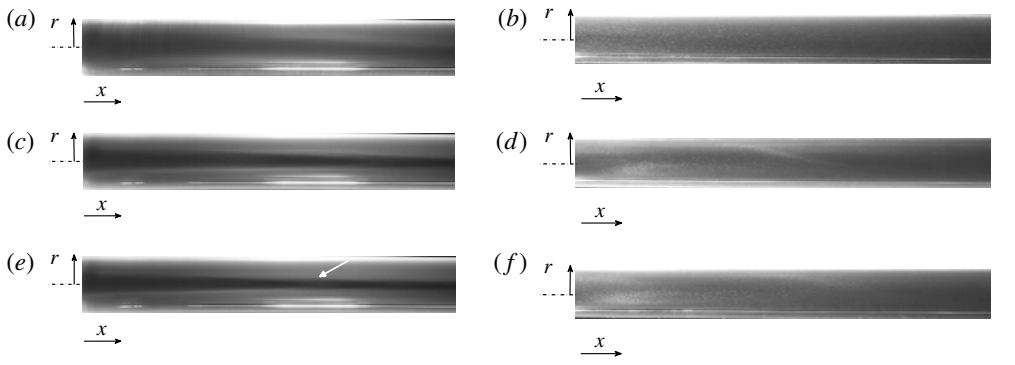

FIGURE 2. Flow visualizations in axial (r, x) planes at the inlet (a,c,e) and downstream regions (b,d,f) for $Re = 250$ and three values of the swirl parameter L: 0.1 (a,b); 1.0 (c,d); and 1.5 (e,f). The flow is stable in (a,b), convectively unstable in (c,d) and (e,f) correspond to a case that theoretically is absolutely unstable. The length of these frames corresponds to approximately $9D$, and they start at $x \simeq 2D$ for (a,c,e), and $x \simeq 84D$ for (b,d,f). We mark in (e) with a white arrow the ACS–SWC transition.

this corresponds to the transition from a convective to an absolute instability of the RHPF.

3.1. *Onset of convective instabilities*

Firstly we focus on the transition from stable to convectively unstable flow, where the visual information in the downstream region allows us to define the transition curve in an (L, Re)-plane, see figure 3. The points depicted in this graph were obtained either for a constant Reynolds number and increasing the parameter L or vice versa. Figure 3 also contains the theoretical neutral curves for the transition from a stable (S) to a convectively unstable state (CI), and for the onset of absolute instabilities (AI), respectively (Fernandez-Feria & del Pino 2002). These theoretical predictions are both for perturbations with an azimuthal wavenumber $n = -1$. Also included in the figure are the theoretical curves for the onset of instabilities with azimuthal wavenumber $n = -2$, which occur for higher values of Re and L. Experimental data are plotted with crosses, circles and stars for the stable, convectively and absolutely unstable cases, respectively (see below for the experimental characterization of the absolutely unstable cases). Good agreement is found between the theoretical curves and the experimental data for the stable to convectively unstable flow transition. Even for very large values of the swirl parameter, no unstable structures were observed with a Reynolds number below 83, confirming Pedley's (1968) critical value of 82.9. On the other hand, even for very high values of Re, no unstable flows were found at low L, when $Re_\theta = ReL$ is below 27. This fact corroborates Mackrodt's (1976) critical swirl Reynolds number of 26.96. For moderate values of the swirl parameter ($0.4 \lesssim L \lesssim 1$) and moderate Reynolds numbers ($Re \approx 100$) there is a small difference between the theoretically predicted transition and the experimental values. This is due to the fact that in this region of the (L, Re)-plane close to the neutral curve, the amplitudes of the linear instabilities were very weak and it was not possible to detect with accuracy the transition by means of the present visualization technique. However, as will be shown below, the experimental frequencies were predicted very accurately.

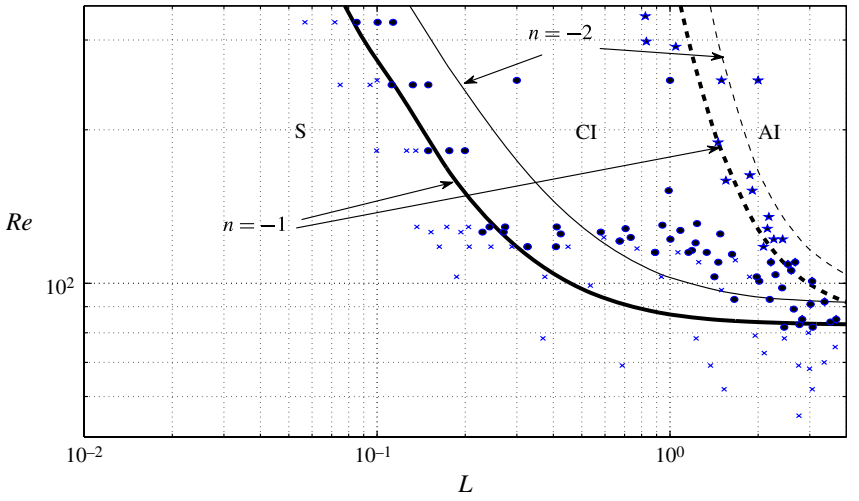

FIGURE 3. Stability diagram in an (L, Re)-plane. Solid and dashed lines represent the theoretical curves for convective and absolute instabilities, respectively. Thick and thin curves correspond to $n = -1$ and $n = -2$, respectively. Experimental data correspond to a stable flow (crosses), and convectively (circles) and absolutely (stars) unstable flows.

Next we focus on how some quantitative data are obtained from flow visualizations. To this end we first obtain spatio-temporal diagrams from a temporal sequence of flow visualization frames, such as those shown in figure 4, corresponding to the same cases depicted in figure 2. In these diagrams, the spatial domain is equal to a stretch of the pipe axis ($r = 0$ and x in the range of the given visualization window), while the temporal evolution of figure 4 only corresponds to $0 \leqslant t \leqslant 40$ s, though the videos analysed were recorded for 90 s. These spatio-temporal diagrams were made by assembling a matrix in which each row corresponds to an image of the stretch of the pipe axis, for successive video images. From these spatio-temporal diagrams we were able to compute both the non-dimensional frequency [$\omega = (\hat{\omega}D)/(4U)$], and the dimensionless axial wavenumber ($\alpha = D\hat{k}/2$), of the instability waves, $\hat{\omega}$ and $\hat{k}$ being the dimensional frequency and wavenumber, respectively. This method has been used successfully in the past to determine unstable structures in stratified Couette flow (Le Bars & Le Gal 2007). There are no flow structures in figure 4(*a,b*), which corresponds to a stable case. However, weak structures appear in figure 4(*d*), which have a negative slope in the (x, t)-plane denoting travelling waves with negative phase velocity. These results, after applying the two-dimensional Fourier transformation to the spatio-temporal diagram of figure 4(*d*), are depicted in figure 5(*d*), where we represent the power spectra in a (ω, α)-plane. The maximum peak is located at (0.802, −0.294), which agrees fairly well with the theoretical frequency and axial wavenumber reported in Fernandez-Feria & del Pino (2002) for the onset of convective instabilities for this value of Re. The agreement for the frequency is much better than for the wavenumber. The reason is that the video was recorded for 90 s and we were able to see several periods of the waves whereas, due to limitations of space and camera resolution, we could only record a pipe length equal to $9D$, approximately. The results of the frequency analysis have a non-dimensional absolute error of 0.016 for

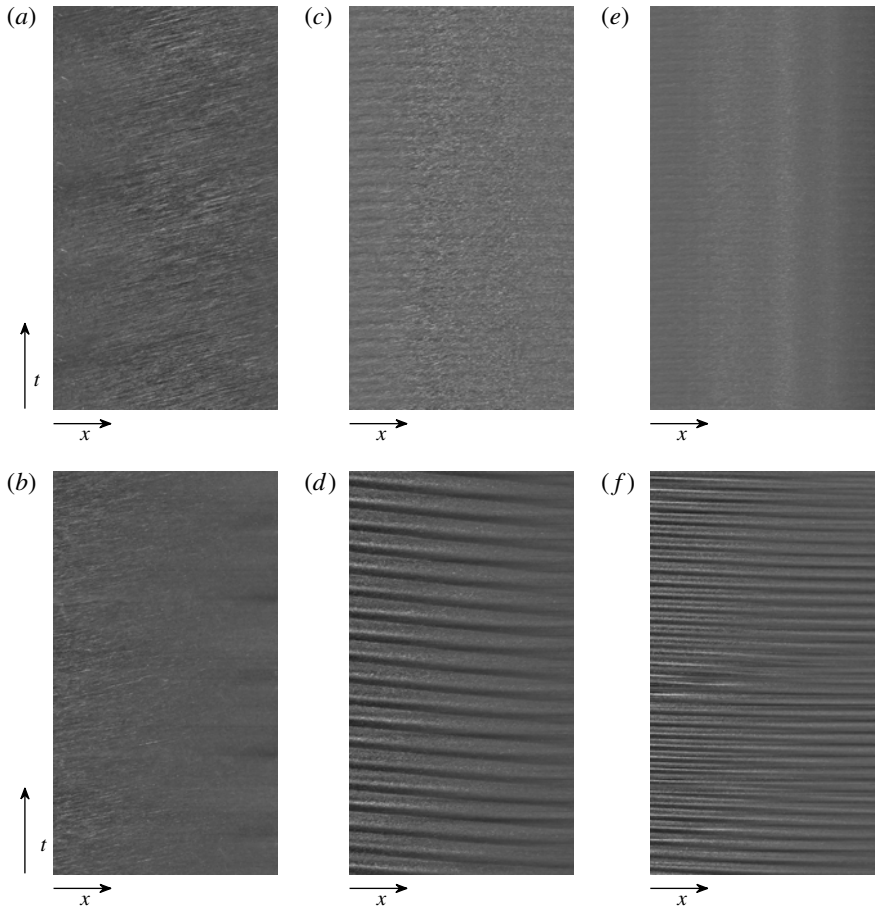

FIGURE 4. Space–time diagrams for $Re = 250$ and three values of the swirl parameter (as in figure 2): $L = 0.1$ (a,b), stable; $L = 1.0$ (c,d), convectively unstable, and $L = 1.5$ (e,f), absolutely unstable for the inlet (a,c,e) and the downstream regions (b,d,f). The time evolution corresponds to $0 \leqslant t \leqslant 40$ s.

the frequency and 0.045 for the wavenumber. As we move outside the most energetic mode, other complex structures appear which correspond to lower energetic ones. However, we will focus only on the most relevant pair of values in the (ω, α)-plane. The stable state, e.g. figure 4(a,b), is characterized for values of both the frequency and wavenumber equal to zero (see figure 5a,b). All this information was also required for better defining the experimental stable–convectively unstable transition in figure 3.

The results thus obtained for the non-dimensional frequency (ω) and wavenumbers (α) against the swirl parameter (L) for the stable–convectively unstable transition, as well as the theoretical predictions for the neutral modes with azimuthal wavenumber $n = -1$, are plotted in figure 6. For simplicity, only representative values for the stable–convectively unstable transition (figure 3) obtained with a constant Re and increasing L are depicted in figure 6. One can observe that a reasonably good agreement is found for the frequency and wavelength in the range $0.5 \lesssim L \lesssim 2$. For

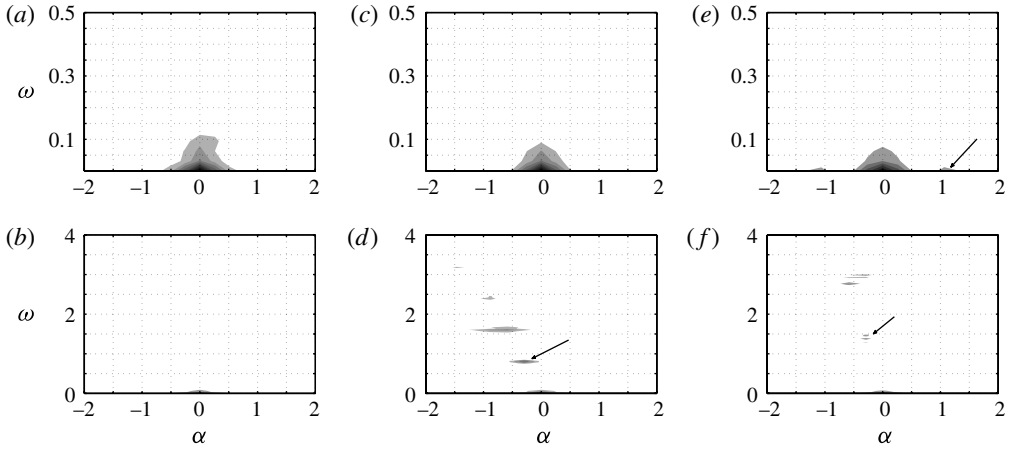

FIGURE 5. Two-dimensional-Fourier power spectra of the space–time diagram for the same cases as figure 4.

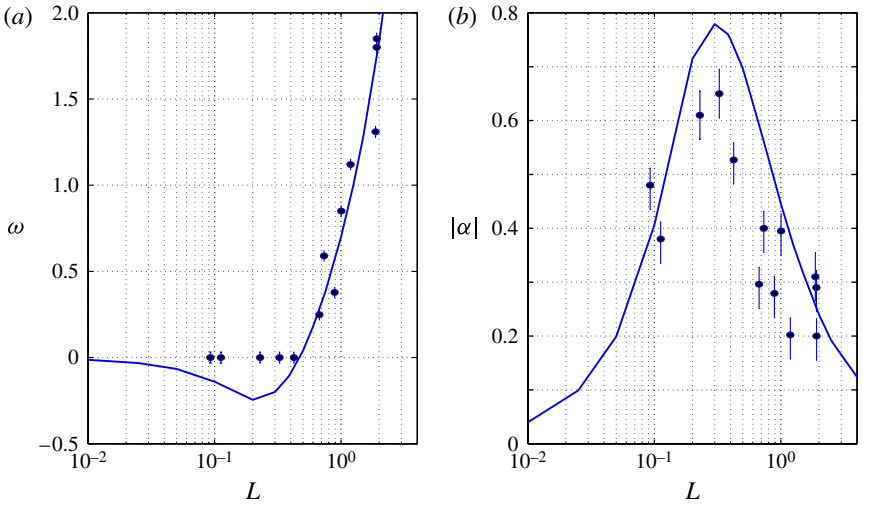

FIGURE 6. Dimensionless theoretical (solid line) and experimental (circles) frequency ω (*a*) and wavelength α (*b*) versus swirl parameter L for the convectively unstable neutral curve of figure 3.

lower values of L, though the wavelengths were in good agreement, zero frequencies were found, showing that the two-dimensional-FFT (fast Fourier transform) offset with these weak waves was not enough to compute the frequency. For $L \gtrsim 2$, disagreement between the theoretical prediction and the measured frequencies or wavenumbers was also found (not shown in figure 6). The explanation is that the pipe was not long enough for developing an RHPF when $L \gtrsim 2$ and Re of the order of 100, as was

discussed above. Finally, it is worth mentioning that the waves described in the spatio-temporal picture of figure 4(*d*) correspond to an azimuthal wavenumber $|n| = -1$, since the diagrams of figure 4 depict the temporal variations of the perturbations in the flow at the axis, which are non-vanishing only for this value of n. This is in agreement with the theoretical predictions for the onset of convective instabilities, which always occur for perturbations with $n = -1$.

3.2. *Absolute instabilities*

Regarding the convective–absolute transition we would have expected to see a qualitative change in the two-dimensional Fourier analysis. However, as is shown in figure 4(*f*), the general structure of the spatio-temporal diagram in the downstream region is similar to that in figure 4(*d*) for a convectively unstable case, and so is the frequency. Another approach would have been to use the experimental version of the linear impulse response (Delbende, Chomaz & Huerre 1998), but due to the rotation of the pipe it was quite difficult to implement it experimentally. For these reasons, to obtain information about the convective-absolute transition we have studied the inlet region ($2D \lesssim x \lesssim 10.5D$), also shown in figures 2 and 4.

Although there are no available theoretical studies, to our knowledge, on global instabilities in a developing RHPF, local stability analysis along the pipe (see e.g. del Pino *et al.* 2003) shows that the onset of instabilities for increasing Re or L is always originated in the downstream region where the RHPF is fully developed. Thus, for convective instabilities, the waves are only visualized in the downstream region, provided that their amplitude becomes large enough to be detected downstream experimentally, but leaving unperturbed the upstream flow (figures 2*c* and 4*c*). However, if the flow becomes absolute unstable as Re or L increases (first in the downstream region where the RHPF is fully established), the perturbation propagates upstream in the pipe, until it is damped in the entrance region, breaking the symmetry of the ACS, and increasingly pervading larger areas of this inlet region as Re or L increases. With our visualization technique we cannot measure the group velocity of the waves, only their phase velocity, but we can detect the onset of absolute instabilities by looking at the inlet region and recording the transition from an ACS to a SWC, as depicted in figure 2(*e*). In addition, one can also observe a significant difference between figures 5(*c*) and 5(*e*). While in the convectively unstable case (figure 5*c*) there is a neat peak at ($\omega = 0$, $\alpha = 0$), the absolutely unstable case (figure 5*e*) shows a non-zero wavenumber α which corresponds to the transition from an ACS to a SWC. Another indication of this transition is the vertical streak pattern observed in figure 4(*e*), denoting spatial oscillations of the flow in the inlet region, which is not present in figure 4(*a,c*). Therefore, this analysis based on the different structures observed in the inlet region, ACS or SWC, has provided us with the possibility of characterizing the star symbols shown in the (L, Re)-plane of figure 3, which agree fairly well with the theoretical predictions for the onset of absolute instabilities (Fernandez-Feria & del Pino 2002), in spite of the fact that nonlinear effects may be relevant when the flow becomes absolutely unstable, which obviously are not taken into account by the theoretical predictions from a linear stability analysis.

Repeating the procedure of obtaining the spatio-temporal diagrams of the pipe axis from a temporal sequence of flow visualization frames in the downstream region (e.g. figure 4*f*), and the two-dimensional-Fourier transformation of these diagrams (e.g. figure 5*f*), one can obtain the results shown in figure 7 for the absolute value of the frequency and the axial wavenumber characterizing the convective–absolute transition.

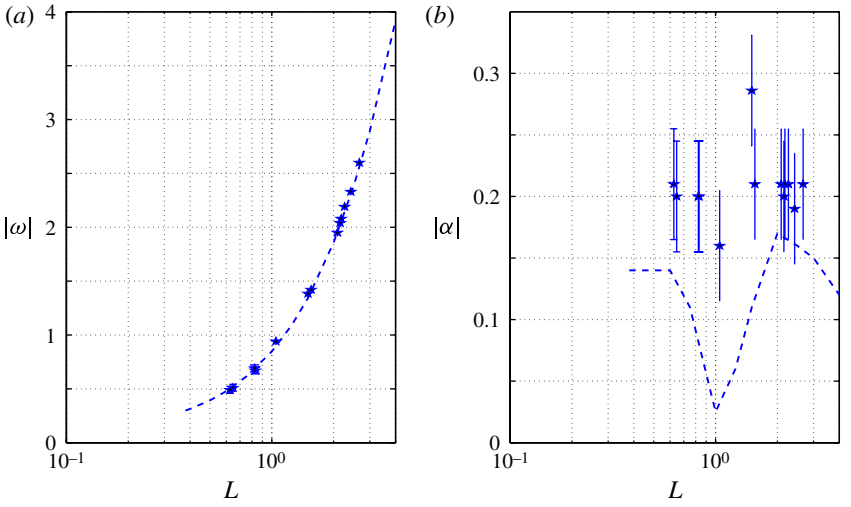

FIGURE 7. Dimensionless theoretical (dashed line) and experimental (stars) absolute value of the frequency ω (a) and wavelength α (b) versus swirl parameter L for the absolutely unstable neutral curve of figure 3.

In these cases, the whole flow oscillated with the absolute frequency, allowing us to measure these quantities in the downstream measurement region. Note in figure 5(f) that the Fourier transformation now shows narrower peaks than in the cases considered in the previous subsection, which constitutes an additional indication of the absolute character of the instability (see Davitian *et al.* 2010 for more details). As before, excellent agreement with the theoretical predictions was found in the case of the frequency, and a reasonably good agreement was found for the axial wavenumbers. These last values were close to 0.1, which means that the waves had a wavelength of $\lambda = \pi D/\alpha \simeq 31.4D$. So in our measurements in the downstream region we were only able to capture about one third of the entire wavelength. Nevertheless the results were of the same order as the theoretical predictions. Finally, it is worth noting that no hysteresis phenomenon was observed.

4. Conclusions

Novel experimental observations related to the RHPF have been reported in this study. Good agreement has been found with the predicted critical values of the Reynolds number and the swirl parameter for both the transition from stable to convectively unstable flow and for the onset of absolute instability. A good agreement was also found with the predicted values of the frequencies and wavelengths of the corresponding travelling waves. A wide range of Reynolds numbers and swirl parameters have been tested, though there was a constraint in this experimental study related to the length of the pipe, which limited the fully developed RHPF to swirl numbers $L \lesssim 2$ for the Reynolds numbers considered.

Experimental evidence of absolute instabilities is given here for the first time for a confined spatially developing forward flow. In those cases, the whole flow was shown to oscillate with the absolute frequency, and the instability modified the flow structure

even in the base flow developing region near the inlet of the pipe, that was supposed to be stable for these values of the parameters. Although an excellent agreement was found here between the experimental frequencies and the theoretically predicted ones for the convective–absolute transition in a fully developed RHPF, further theoretical and numerical work on the absolute instability of the whole developing flow that takes into account nonlinear and non-local effects is required.

Acknowledgements

The authors would like to thank the anonymous reviewers for their valuable comments to improve the original version of the manuscript. We also thank S. Pinazo his technical support.

References

ARIYARATNE, C. & JONES, T. F. 2007 Design and optimization of swirl pipe geometry for particle–laden liquids. *AIChE J.* **53** (4), 757–768.

BARNES, D. R. & KERSWELL, R. R. 2000 New results in rotating Hagen–Poiseuille flow. *J. Fluid Mech.* **417**, 103–126.

COTTON, F. W. & SALWEN, H. 1981 Linear stability of rotating Hagen–Poiseuille flow. *J. Fluid Mech.* **108**, 101–125.

DAVITIAN, J., GETSINGER, D., HENDRICKSON, C. & KARAGOZIAN, A. R. 2010 Transition to global instability in transverse jet shear layers. *J. Fluid Mech.* **661**, 294–315.

DELBENDE, I., CHOMAZ, J.-M. & HUERRE, P. 1998 Absolute/convective instabilities in the Batchelor vortex: a numerical study of the linear impulse response. *J. Fluid Mech.* **355**, 229–254.

FERNANDEZ-FERIA, R. & DEL PINO, C. 2002 The onset of absolute instability of rotating Hagen–Poiseuille flow: a spatial stability analysis. *Phys. Fluids* **14** (9), 3087–3097.

HEATON, C. J. 2008 On the inviscid neutral curve of rotating Poiseuille pipe flow. *Phys. Fluids* **20**, 024105.

HOF, B., WESTERWEEL, J., SCHNEIDER, T. B. & ECKHARDT, B. 2006 Finite lifetime of turbulence in shear flows. *Nature* **443**, 59–62.

HOSSAIN, K. N., JACKSON, T. L. & BUCKMASTER, J. D. 2009 Numerical simulations of flame patterns supported by a spinning burner. *Proc. Combust. Inst.* **32**, 1209–1217.

HUERRE, P. & MONKEWITZ, P. A. 1990 Local and global instabilities in spatially developing flows. *Annu. Rev. Fluid Mech.* **22**, 473–537.

IMAO, S., ITOH, M., YAMADA, Y. & ZHANG, Q. 1992 The characteristics of spiral waves in an axially rotating pipe. *Exp. Fluids* **12**, 277–285.

LE BARS, M. & LE GAL, P. 2007 Experimental analysis of the strato-rotational instability in a cylindrical Couette flow. *Phys. Rev. Lett.* **99**, 064502.

MACKRODT, P. A. 1976 Stability of Hagen–Poiseuille flow with superimposed rigid rotation. *J. Fluid Mech.* **73**, 153–164.

NAGIB, H. M., LAVAN, Z. & FEJER, 1971 Stability of pipe flow with superposed solid body rotation. *Phys. Fluids* **14**, 766–768.

PEDLEY, T. J. 1968 On the instability of rapidly rotating shear flows to non-axisymmetric disturbances. *J. Fluid Mech.* **31**, 603–607.

PEDLEY, T. J. 1969 On the instability of viscous flow in a rapidly rotating pipe. *J. Fluid Mech.* **35**, 97–115.

DEL PINO, C., ORTEGA-CASANOVA, J. & FERNANDEZ-FERIA, R. 2003 Nonparallel stability of the flow in an axially rotating pipe. *Fluid Dyn. Res.* **32**, 261–281.

SANMIGUEL-ROJAS, E. & FERNANDEZ-FERIA, R. 2005 Nonlinear waves in the pressure driven flow in a finite rotating pipe. *Phys. Fluids* **17**, 014104.

SANMIGUEL-ROJAS, E. & FERNANDEZ-FERIA, R. 2006 Nonlinear instabilities in a vertical pipe flow discharging from a cylindrical container. *Phys. Fluids* **18**, 024101.

TOPLOSKY, N. & AKYLAS, T. R. 1988 Nonlinear spiral waves in rotating pipe flow. *J. Fluid Mech.* **148**, 39–54.

WHITE, A. 1964 Flow of a fluid in an axially rotating pipe. *J. Mech. Engng Sci.* **6**, 47–52.